Supporting Information for

Ultra-Low Density, Monolithic WS_2, MoS_2, and MoS_2/Graphene Aerogels

Marcus A. Worsley*, Swanee J. Shin, Matthew D. Merrill, Jeremy Lenhardt, Art J. Nelson, Leta Y. Woo, Alex E. Gash, Theodore F. Baumann, Christine A. Orme

Lawrence Livermore National Laboratory, 7000 East Ave, Livermore, CA, 94550 USA.
*corresponding author: worsley1@llnl.gov

Supporting Methods

Electrochemical Characterization. All electrochemical tests (CVs, EIS, and LP) were performed in 0.5 M H_2SO_4 using a BioLogic SP300 potentiostat. Solutions were purged with argon gas (99.99999%) for at least 20 minutes before testing and for the duration of the measurements. All measurements used iR compensation. Typical resistances were 4-6 ohms. In addition, non-faradaic contributions to the current are estimated for the monolith samples and subtracted before extracting performance metrics. The working electrodes, counter electrodes and reference electrodes are described below.

Note: Only the monoliths prepared on a graphene backbone are sufficiently conductive to perform electrochemical testing while in the monolithic form. Below we describe cyclic voltammetry (CV), impedance (EIS), and linear polarization stability tests (LP) on the MoS_2/GMA monolith. To compare the conductive MoS_2/GMA with non-conductive MoS_2 and WS_2 materials, all aerogels were made into inks and dispersed as thin layers on a rotating disk electrode (RDE). These thin layers delaminated over time due to the mechanical action of the hydrogen bubbles and did not perform well in stability tests likely due to the very small loading. For this reason only CVs, impedance and initial linear polarization data are shown for these materials.

Working Electrodes: Thin films for RDE. Four inks (graphene aerogel, MoS_2/GMA, MoS_2 aerogel, and WS_2 aerogel) were made using 5 mg aerogel per 5 ml dimethylformamide with 20 µl 5% Nafion (Aldrich 117 Solution). Inks were tip sonicated for 1 minute at 20% power level. A total of 20 µl of ink was allowed to dry under vacuum on a 5mm diameter glassy carbon (GC) electrode (Pine Instruments). Glassy carbon electrodes (Pine Instruments) were polished using 0.05 µm colloidal silica and sonicated in ethanol between each use. This process creates thin film electrodes with 12 µg of aerogel over an area of 0.196 cm^2, corresponding to a loading of ~60 µg/cm^2. A polished platinum disk (5 mm diameter) electrode (Pine Instruments AFE5T050PT) was used the Pt catalyst sample.

Reference and Counter Electrodes: RDE studies. RDE studies we used a 99.9995% graphite counter electrode (Alfa Aesar 14738) and a single junction $Hg/HgSO_4$ reference electrode (Hach XR200) with 0.5M H_2SO_4 fill solution. The $Hg/HgSO_4$ reference was checked against an unused set of electrodes before and after each run to ensure that the value did not drift more than +- 0.0015 V. Plots are referenced with respect to the reversible hydrogen electrode (RHE). The RHE offset was measured as the open circuit potential difference between the $Hg/HgSO_4$ electrode and a Pt electrode in 0.5 M H_2SO_4 solution purged with 100% H_2. The offset with respect to normal hydrogen electrode (NHE) was estimated from the solution pH = 0.44+-0.02 using, VRHE= VNHE – 0.059 * pH. The pH was measured using a freshly calibrated double junction pH probe (Accumet model 13-620-183a). Numerically, V(RHE) = V($Hg/HgSO_4$) + 0.683 and V(RHE) = VNHE - 0.026 +-0.001. (The pH is shifted compared to the monolith studies due to batch-to-batch variation in preparing the solution).

Note: High surface area aerogel foams are efficient getters and readily adsorb metal ions from solution. We found that if we used a platinum counter electrode or a single junction reference electrode we had ~10 atomic percent Pt and ~5 atomic percent Hg after 48 hours of cycling (as measured by XPS). The platinum adsorption led to artificially high HER activity. We note that it is standard practice to exchange solutions for fresh solution at the end of a stability/aging experiment to ensure that changes to the solution are not responsible for electrochemical response. This is not a sufficient test for these high surface area materials as they adsorb contaminates leaving the solution free of metal contaminants. Due to these issues, all data shown in this paper used a graphite counter electrode and are free from possible platinum contamination. In addition, for stability tests we use a double junction reference electrode to avoid Hg contamination.

Supporting Figures

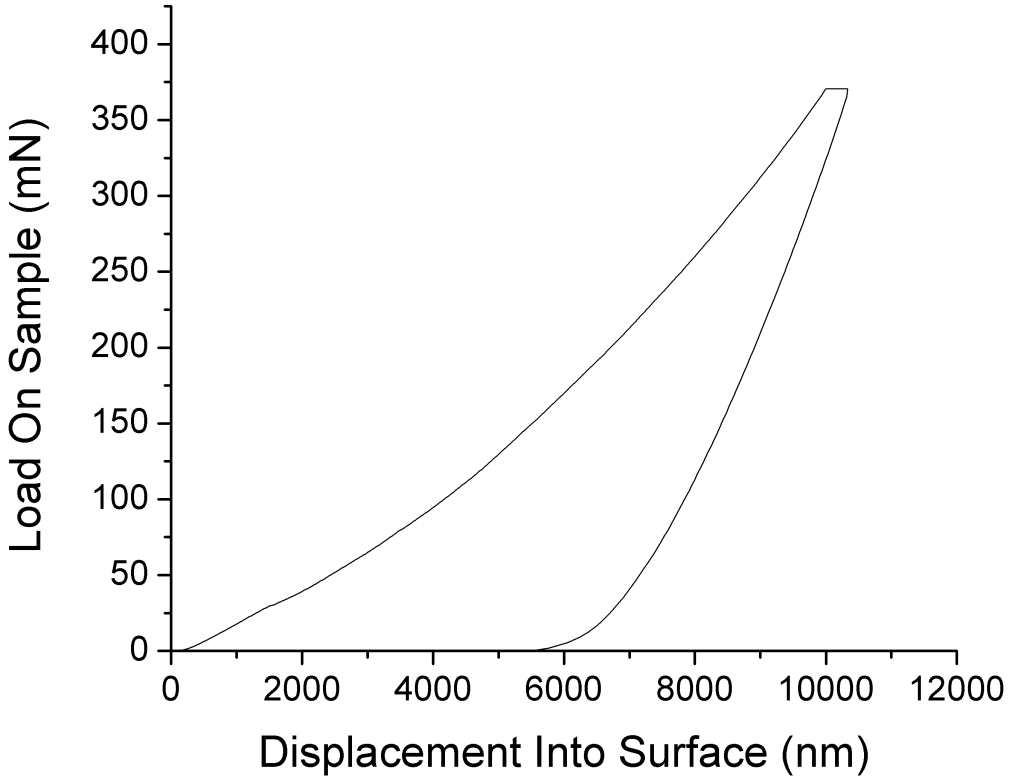

Figure S1. Representative load *vs.* displacement plot for dichalcogenide aerogels (54 mg/cm^3 WS_2 aerogel).

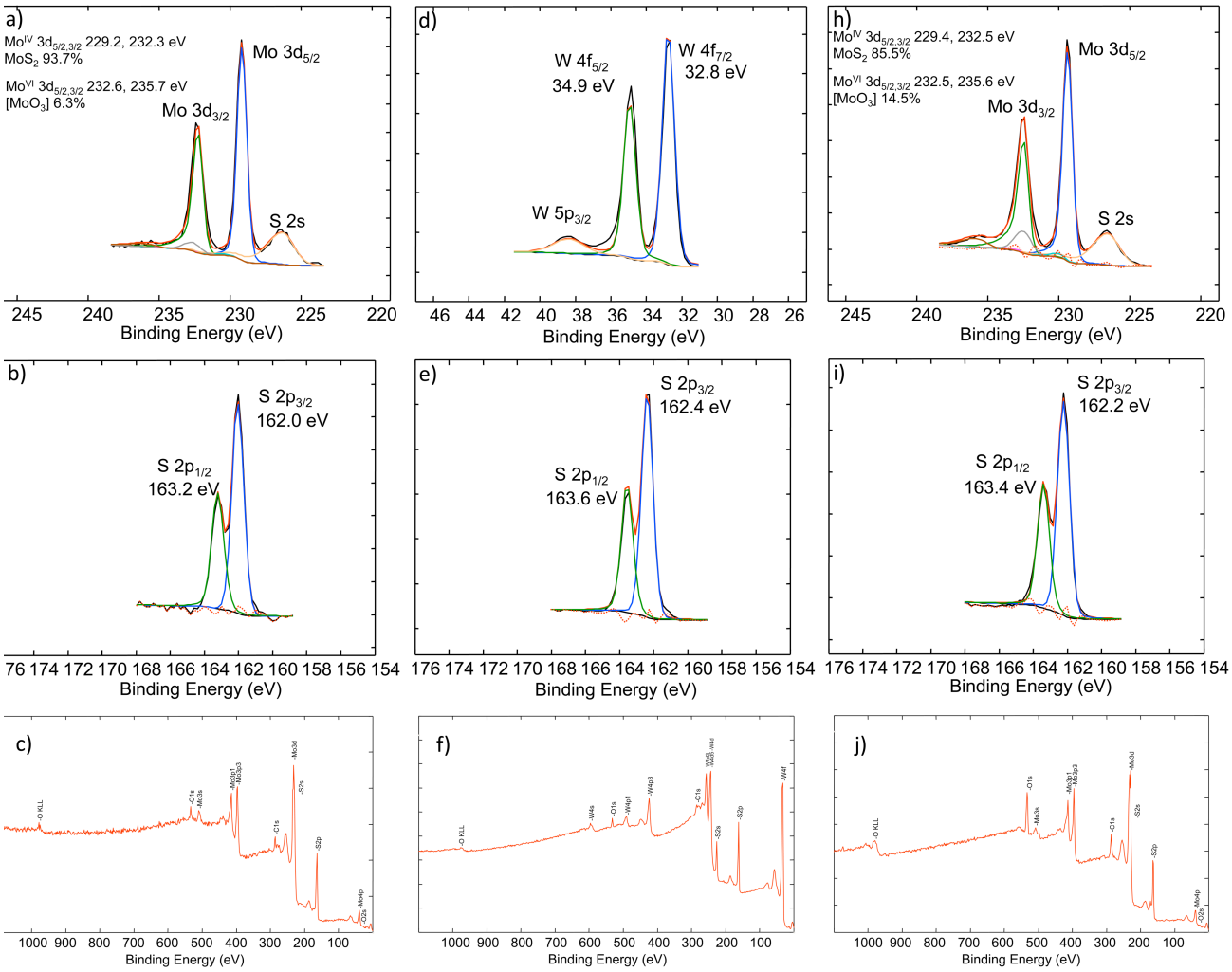

Figure S2. XPS spectra for a) Mo 3d peaks (MoS_2), b) S 2p peaks (MoS_2), d) 4f peaks (WS_2), e) S 2p peaks (WS_2), h) Mo 3d peaks (MoS_2/GMA) and i) S 2p (MoS_2/GMA). XPS survey spectra for c) MoS_2, f) WS_2, and j) MoS_2/GMA aerogels.

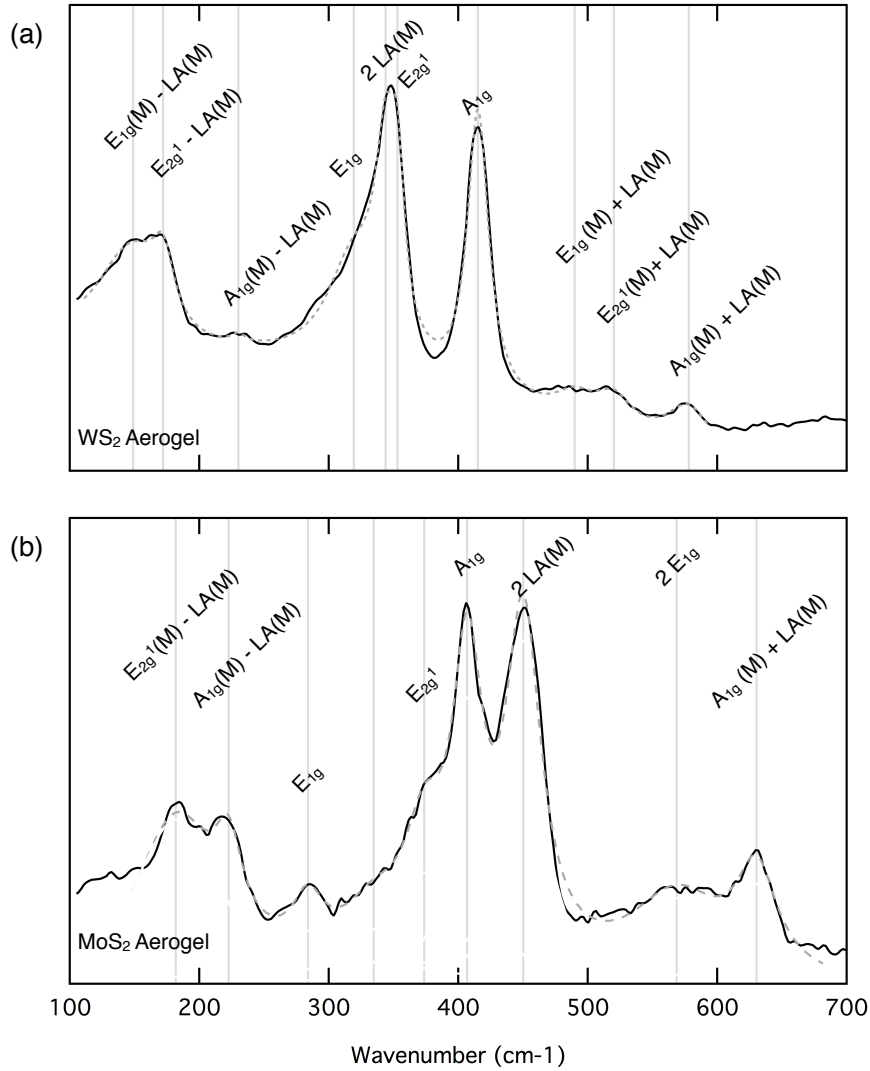

Figure S3. Raman spectra with 633nm excitation for a) WS_2 aerogel and b) MoS_2 aerogel. MoS_2 resonant modes are consistent with LA(M) 233 cm^{-1} coupled with A_{1g}(M) (408 cm^{-1}), E_{1g} (M) (286 cm^{-1}), and E_{2g}^1(M) (383 cm^{-1}). WS_2 resonant modes as identified in figure are consistent with LA(M) 175 cm^{-1} coupled with A_{1g}(M) (406 cm^{-1}), E_{1g} (M) (320 cm^{-1}), and E_{2g}^1(M) (345 cm^{-1}).

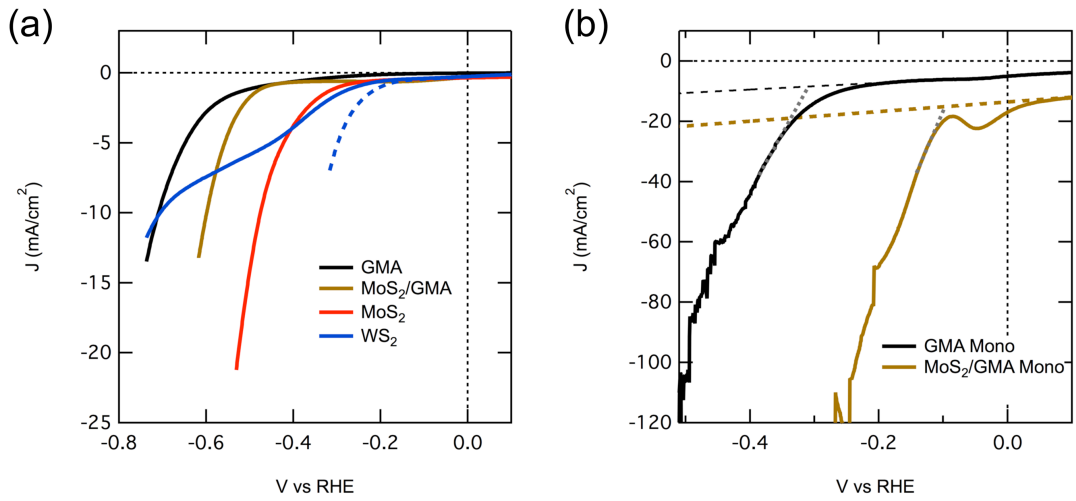

Figure S4. Linear polarization curves (current density normalized by geometric area versus potential) of the (a) thin film and (b) monoliths. The thin films have substantially higher onset potentials than the monoliths. WS_2 changes within the first few scans; the first (dotted) and fifth (solid) scan are shown. (b) The non-faradaic corrections (dashed lines near horizontal) are shown for each sample along with the extrapolation (near vertical) used to estimate the onset voltage.

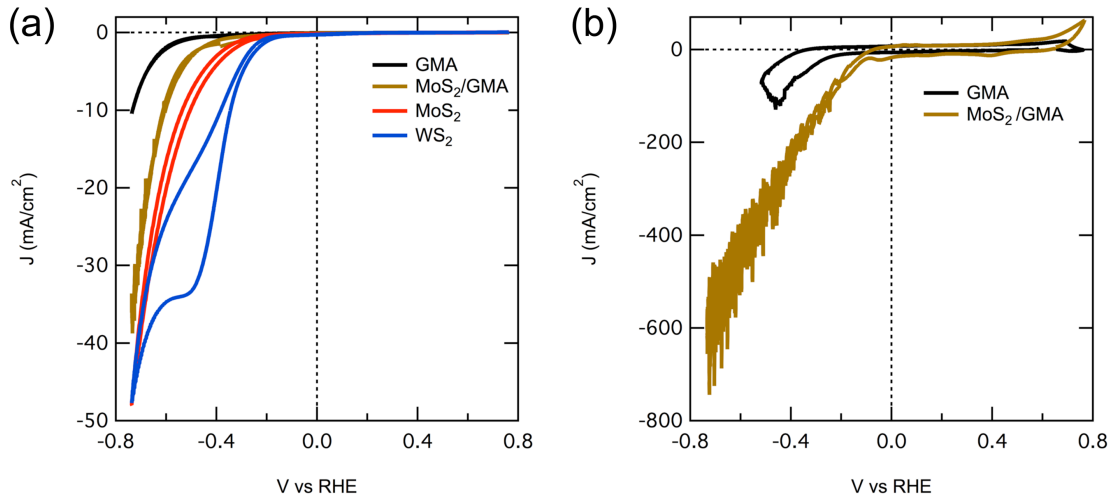

Figure S5: (a) Cyclic voltammograms of the thin film electrodes with 12 μg of material rotating at 2500 RPM. Scan rates were 2 mV/s except the MoS_2 sample, which was 10 mV/s. The MoS_2/GMA sample is noisy due to trapped hydrogen bubbles. (b) CVs of monoliths performed at 2 mV/s scan rate. Current density normalized to geometric area.

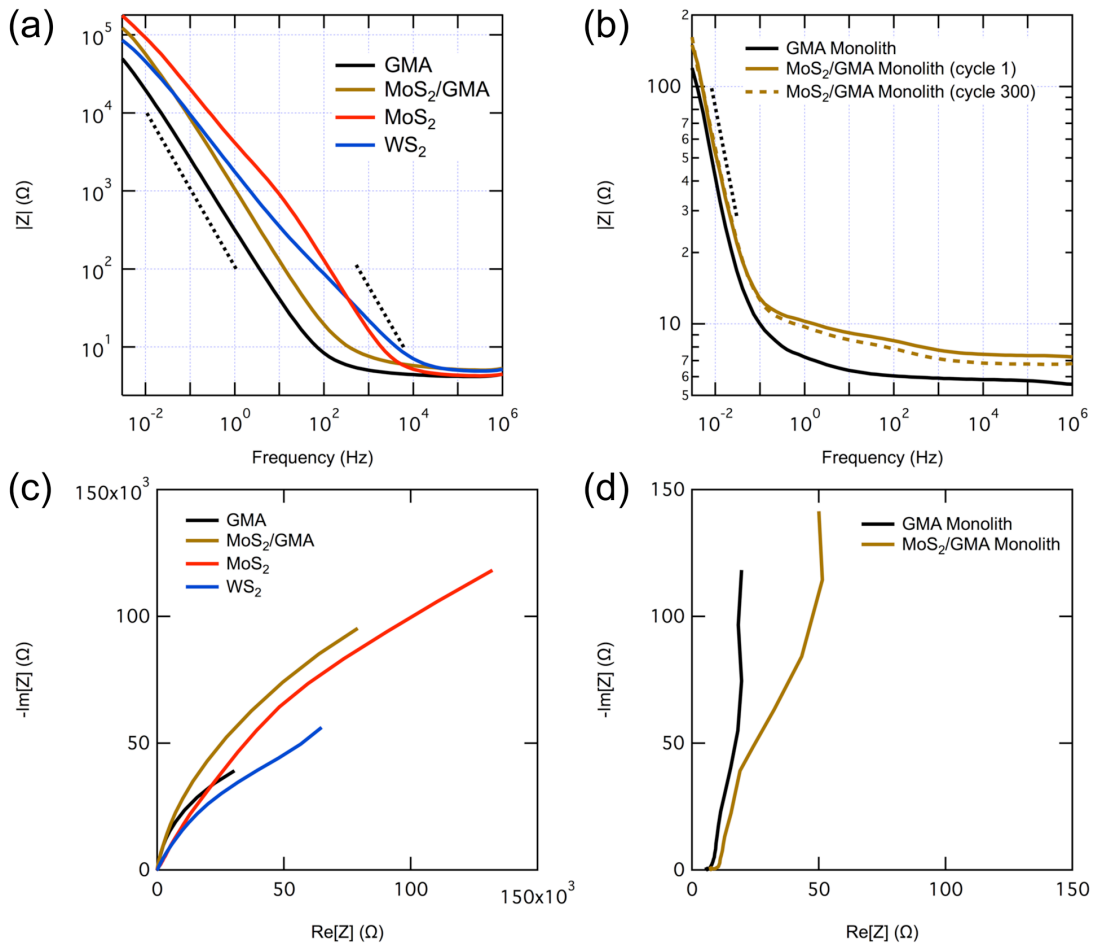

Figure S6: (a) Bode plots of four films are composed of graphene aerogel (black) MoS_2/GMA (brown), MoS_2 (red) and WS_2 (blue) measured at 0.56 V *vs.* RHE. Dashed lines and grid indicate a slope of 1/f. (b) Bode plots of the two conductive monoliths, GMA (black) and MoS_2/GMA (brown) at 0.56 V *vs.* RHE. Bode plots before (solid) and after (dashed) cycling have similar capacitances indicating that the surface area is not changing significantly. Corresponding Nyquist plots of (c) thin films and (d) monoliths.

Discussion

Nanoindentation. A representative load *vs.* displacement plot for dichalcogenide aerogels is shown in Figure S1. Note that indentation was held at maximum load for 10 seconds to minimize time dependent plastic effects in unloading curve. [1] Calculated Young's modulus is 35±5 MPa, which is comparable to values reported in analogous graphene aerogels.[2] Large residual impression after the loading cycle and creep during the hold period indicate plastic deformations occur and some of them are time dependent. The deformation mechanism could involve dislocation motions, which are commonly observed in full density metals such as aluminum and tungsten[1] and brittle fracture of the ligaments

accompanied by pore collapse, which is dominant in low-density brittle nanoporous solids. [3]

*X-ray Photoelectron Spectroscopy.*_XPS results (Figure S2) for the S 2p peaks in MoS_2 and WS_2 aerogels are consistent with S^{2-} typical of MoS_2 and WS_2. According to XPS analysis, 86% of the Mo 3d signal in the hybrid aerogel is due to Mo(IV) species in MoS_2 (Mo $3d_{5/2}$, BE = 229.4 eV). The remainder is due to MoO_3, likely from oxidation upon exposure to air. Nearly 100% of the sulfur is due to S^{2-} (S $2p_{3/2}$, BE = 162.2 eV) typical of MoS_2.

Raman Spectroscopy. The aerogels were examined by resonant Raman spectroscopy (Figure S3). Spectra are consistent with randomly oriented nanocrystalline MoS_2 and WS_2 composed of multiple layers of MoS_2 and single (or decoupled) layers of WS_2.

Bulk MoS_2 and WS_2 are in the hexagonal crystal system with space group P63/mmc and international point group 6/mmm (Schonflies point group D6h). Materials with this symmetry can have first order Raman processes designated as A_{1g}, E_{1g}, E_{2g}^1, and E_{2g}^2 as well as acoustic modes.[4] The A-modes represent vibrations perpendicular to the basal plane whereas the E-modes are vibrations within the basal plane. In addition to the primary modes, resonant Raman effects are observed due to the coupling of these modes with the longitudinal acoustic mode, which previous studies identify as LA(M), an acoustic mode in the M-direction of the Brillouin zone.[5]

MoS_2 Aerogel: The literature describes MoS_2 Raman spectra for bulk single crystals as well as spectral changes due to small domain size and small layer thickness. The major peaks found for the MoS_2 aerogel are A_{1g} (407 cm^{-1}), E_{1g} (284 cm^{-1}), E_{2g}^1 (374 cm^{-1}) along with 2xLA(M) at ~450 cm^{-1}. These peak positions are in good agreement with literature values for nanoparticulate MoS_2 that is composed of multiple layers (rather than monolayer).

Small basal domain size and disorder tend to broaden and soften in-plane (E) phonon modes and to increase acoustic scattering at grain boundaries compared to bulk values. All of these effects are apparent in the aerogel spectra. First, the symmetric bending mode, E_{2g}^1 measured at 374 cm^{-1} is red-shifted by 9 cm^{-1} from the bulk value at 383 cm^{-1}. Second, we observe a strong 2xLA(M), which is associated with disorder in the basal plane. Lastly the relative amplitude ratio of the A_{1g}/ E_{2g}^1 is 2.2 for the aerogels compared with <1.5 for bulk crystals, a trend that has been demonstrated for nanoparticles.[6] The primary signature of monolayer versus multilayer films is a softening of the A_{1g} mode. The aerogel values are intermediate between bulk values (408 cm^{-1}) and monolayer values (405 cm^{-1}), i.e in the range of 2-10. TEM images confirm nanoparticles with a 5-10 nm domain size and 2-8 monolayers thick.

WS_2 Aerogel: WS_2 is less well studied than MoS_2 but data from bulk and few-layer films have been reported.[7-10] The major peaks found for the WS_2 aerogel are A_{1g} (415 cm^{-1}), E_{1g} (tentatively at 319 cm^{-1}), E_{2g}^1 (353 cm^{-1}) and the 2x harmonic of LA(M) at ~340 cm^{-1}. In comparing with MoS_2, E_{2g}^1, which involves a M-S vibration, is lower due to the higher molecular weight of tungsten. Similarly the longitudinal acoustic mode, which depends on the crystal effective mass, is lower. By contrast, modes that involve vibrations between nearby sulfur atoms (A_{1g} and E_{1g}) are stiffer for WS_2.

The peak position for the A_{1g} mode, which is the strongest indicator of coupling between layers, is consistent with literature reports for exfoliated (monolayer) flakes. However, our TEM images suggest that particles are composed of multiple layers. Together these findings are consistent with stacked flakes that are less coupled (farther apart) than bulk. The peak assigned to A_{1g} may also have a B_{2u} component.[10] This would explain the difference between the peak value near 415 cm^{-1} and the positions of the resonant peaks A_{1g} +- LA(M), which are consistent with a lower value (Figure S3). There are few experimental reports[11] for the in plane, E_{1g} mode of WS_2 because most studies have used crystals oriented perpendicular to the laser beam, which does not excite this mode. It has been calculated[12] to be near 287 cm^{-1}. and measured[11] at 306 cm^{-1}. Our value at 319 cm^{-1} is higher than predicted and because there are also small resonant peaks in this region,[5, 13] an off-resonance Raman spectra is needed to conclusively assign this peak.

Table S1. Comparison between Raman modes of aerogels and literature bulk values

Primary Mode	**MoS_2 Aerogel**	**MoS_2 (Bulk)[4, 6, 9, 14-17]**	**MoS_2 Monolayer[7, 13, 18]**	**WS_2 Aerogel**	**WS_2 (Bulk)[8, 11]**	**WS_2 Monolayer[5, 7, 10, 19]**
E_{2g}^2(G)		32			27	
LA(M)	223	233		172	176	176
E_{1g}	284	286		319		
E_{2g}^1	374	383	377-385	353	355-356	350-356
A_{1g}	407	408	405	415	420	415-418

Electrochemical Characterization. Linear polarization curves (Figure S4) were used to extract performance metrics such as the onset potential for hydrogen

evolution and the potential needed to achieve specific current densities. These are provided in Table S2. The presence of a redox peak near the onset of hydrogen evolution prevented a Tafel representation of the data.

Although all data is iR-corrected (during data collection) to compensate for solution and instrumentation effects, additional corrections are needed to account for non-Faradiac contributions of the monolithic samples. Non-faradaic contributions to the current were estimated and subtracted from the total current to provide performance metrics. The subtracted current was estimated as $I_{NF} = C\frac{dV}{dt} + \frac{V - V_{OCP}}{R_2}$ where C is the capacitance, V is the applied potential, V_{OCP} is the open circuit potential, R_2 is a resistor in parallel with the capacitor and dV/dt is the scan rate (and is negative for data shown). This analysis uses impedance data and assumes a Randles circuit where the capacitance and resistance are independent of voltage (Table S2). For the monoliths, J_{NF}~10 mA/cm^2 at the onset of hydrogen evolution. These effects are much smaller and ignored for the thin film samples. After subtracting non-faradaic contributions, the voltage needed to generate 10 mA/cm^2 is -0.12 V and the voltage needed to generate 100 mA/cm^2 is -0.26 V *vs.* RHE (Table S2). Due to the presence of a redox peak near the onset of hydrogen evolution the onset potential was chosen by extrapolation from the near vertical portion of the curve rather than the near horizontal curve (as is more common in the literature). This shifts the onset potential to a more negative value. The same procedure was used for both RDE and monolithic samples to aid comparison. The peaks may correspond to Mo or S redox activity or H adsorption.

Exemplary cyclic voltammograms of the four thin film electrodes within the first 10 cycles. (Figure S5) The potential needed to generate a current density of 10 mA/cm^2 was -0.73, -0.60, -0.50, and -0.34 V *vs.* RHE for GMA, MoS_2/GMA, MoS_2, and WS_2 electrodes, respectively. However this performance degraded over time. The monoliths with higher loading and more mechanically robust structures performed better with cycling.

EIS measurements were used to characterize monolith and film capacitance. AC impedance measurements were carried out at 0.56 V *vs.* RHE from 20 mHz to 1 MHz with an AC voltage of 10 mV. Thin film samples were rotated at 2500 RPM.

EIS data is shown in the form of a Bode and Nyquist plots at a potential of 0.56 *vs.* RHE where no redox reactions are observed. (Figure S6) The GMA and MoS_2/GMA substrates are dominated by a capacitive impedance due to their high surface areas and thus have slopes near 1/f (dashed line). MoS_2/GMA has higher electron transfer resistance than pure GMA as demonstrated by the higher impedance at low frequency and the right shift of the impedance node near 100 Hz. These are consistent with a MoS_2 coating on graphene. The pure MoS_2 and WS_2 aerogels have lower surface areas and corresponding lower capacitance values. The MoS_2 aerogel sample has two slopes (near 1/f and 2/f)

indicating multiple types of active interfaces. The capacitance is estimated by averaging over the 1/f region of Bode plots using $C = 1/2\pi f|Z|$, giving values of 2.7, 0.6, and 0.08 mF/cm^2 for GMA, MoS_2/GMA, and MoS_2 thin films respectively. WS_2 has more complex impedance behavior and could not be estimated in this manner.

Figure S6 also shows EIS data for monoliths, which have lower electron transfer resistance and higher capacitance than the thin film samples. For monoliths C_{GA} = 0.40+- 0.04 F and $C_{MoS2\text{-}GMA}$ = 0.28 +- 0.04 F averaged over the frequency range 0.004 – 0.04 Hz. The capacitance is unchanged after 300 cycles. The corresponding specific capacitances are $C_{s,GMA}$ = 2.0+-0.2 F/cm^2 and $C_{s,\ MoS2/GMA}$ = 1.4+-0.2 F/cm^2, respectively. These values are in agreement with best fits assuming a Randles circuit.

Table S2. Monolith performance metrics: Onset voltage, voltage needed to achieve 10 and 100 mA/cm^2. Lumped circuit values used to subtract the non-faradaic contributions. Voltages provided versus RHE.

	R1 (ohms)	**R2 (ohms)**	**C (F)**	**V_{OCP}**	**V_{onset}**	**V_{10}**	**V_{100}**
GMA Monolith	6	460	0.4	0.09	-0.31	-0.33	-0.50
MoS_2/GMA Monolith	8	320	0.31	0.65	-0.10	-0.12	-0.26
GMA					-0.53	-0.71	
MoS_2/GMA					-0.47	-0.60	
MoS_2					-0.28	-0.48	
WS_2					-0.18/ -0.24	-0.34/ -0.70	

References

1. W. C. Oliver and G. M. Pharr, An Improved Technique for Determining Hardness and Elastic-Modulus Using Load and Displacement Sensing Indentation Experiments, *J. Mater. Res.* **1992,** 7, 1564-1583.
2. M. A. Worsley, S. O. Kucheyev, H. E. Mason, M. D. Merrill, B. P. Mayer, J. Lewicki, C. A. Valdez, M. E. Suss, M. Stadermann, P. J. Pauzauskie*, et al.*, Mechanically Robust 3D Graphene Macroassembly with High Surface Area, *Chem. Commun.* **2012,** 48, 8428-8430.
3. S. O. Kucheyev, A. V. Hamza, J. H. Satcher and M. A. Worsley, Depth-Sensing Indentation of Low-Density Brittle Nanoporous Solids, *Acta Mater.* **2009,** 57, 3472-3480.
4. T. Wieting and J. Verble, Infrared and Raman Studies of Long-Wavelength Optical Phonons in Hexagonal MoS_2, *Phys. Rev. B* **1971,** 3, 4286-4292.

5. A. Berkdemir, H. R. Gutiérrez, A. R. Botello-Méndez, N. Perea-López, A. L. Elías, C.-I. Chia, B. Wang, V. H. Crespi, F. López-Urías and J.-C. Charlier, Identification of Individual and Few Layers of WS_2 Using Raman Spectroscopy, *Sci. Rep.* **2013,** 3.
6. G. Frey, R. Tenne, M. Matthews, M. Dresselhaus and G. Dresselhaus, Raman and Resonance Raman Investigation of MoS_2 Nanoparticles, *Phys. Rev. B* **1999,** 60, 2883-2892.
7. M. Ramakrishna, A. Gomathi and A. Manna, MoS_2 and WS_2 Analogues of Graphene., *Angew. Chem. Int. Ed.* **2010,** 49, 4059–4062.
8. C. Sourisseau, M. Fouassier, M. Alba, A. Ghorayeb and O. Gorochov, Resonance Raman, Inelastic Neutron Scattering and Lattice Dynamics Studies of 2H-WS_2, *Mater. Sci. Eng., B* **1989,** 3, 119-123.
9. A. Stacy and D. Hodul, in *J. Phys. Chem. Solids* (1985), Vol. 46, pp. 405-409.
10. W. J. Zhao, Z. Ghorannevis, K. K. Amara, J. R. Pang, M. Toh, X. Zhang, C. Kloc, P. H. Tan and G. Eda, Lattice Dynamics in Mono- and Few-Layer Sheets of WS_2 and WSe_2, *Nanoscale* **2013,** 5, 9677-9683.
11. M. Virsek, A. Jesih, I. Milosevic, M. Damnjanovic and M. Remskar, Raman Scattering of the MoS_2 and WS_2 Single Nanotubes, *Surf Sci.* **2007,** 601, 2868-2872.
12. M. Ghorbani-Asl, N. Zibouche, M. Wahiduzzaman, A. F. Oliveira, A. Kuc and T. Heine, Electromechanics in MoS_2 and WS_2: Nanotubes Vs. Monolayers, *Sci. Rep.* **2013,** 3.
13. J.-H. Fan, P. Gao, A.-M. Zhang, B.-R. Zhu, H.-L. Zeng, X.-D. Cui, R. He and Q.-M. Zhang, Resonance Raman Scattering in Bulk 2H-MX_2 (M = Mo, W; X = S, Se) and Monolayer MoS_2, *J. Appl. Phys.* **2014,** 115, 053527.
14. T. Sekine, K. Uchinokura and T. Nakashizu, Dispersive Raman Mode of Layered Compound 2H-MoS_2 under the Resonant Condition, *J. Phys. Soc. Jpn.* **1984**, 811-818.
15. B. C. Windom, W. G. Sawyer and D. W. Hahn, A Raman Spectroscopic Study of MoS_2 and MoO_3: Applications to Tribological Systems, *Tribol. Lett.* **2011,** 42, 301-310.
16. J. L. Verble, T. J. Wietling and P. R. Reed, Rigid-Layer Lattice Vibrations and Van Der Waals Bonding in Hexagonal MoS_2, *Solid State Commun.* **1972,** 11, 941-944.
17. J. M. Chen and C. S. Wang, Second Order Raman Spectrum of MoS_2, *Solid State Commun.* **1974,** 14, 857-860.
18. Y. Zhan, Z. Liu, S. Najmaei, P. M. Ajayan and J. Lou, Large Area Vapor Phase Growth and Characterization of MoS_2 Atomic Layers on SiO_2 Substrate, *Small* **2012,** 8, 966-971.
19. J. G. Song, J. Park, W. Lee, T. Choi, H. Jung, C. W. Lee, S. H. Hwang, J. M. Myoung, J. H. Jung, S. H. Kim*, et al.*, Layer-Controlled, Wafer-Scale, and Conformal Synthesis of Tungsten Disulfide Nanosheets Using Atomic Layer Deposition, *ACS Nano* **2013,** 7, 11333-11340.